SENSORS

Printed synaptic transistor–based electronic skin for robots to feel and learn

Fengyuan Liu, Sweety Deswal, Adamos Christou, Mahdieh Shojaei Baghini, Radu Chirila, Dhayalan Shakthivel, Moupali Chakraborty, Ravinder Dahiya*

An electronic skin (e-skin) for the next generation of robots is expected to have biological skin-like multimodal sensing, signal encoding, and preprocessing. To this end, it is imperative to have high-quality, uniformly responding electronic devices distributed over large areas and capable of delivering synaptic behavior with long- and short-term memory. Here, we present an approach to realize synaptic transistors (12-by-14 array) using ZnO nanowires printed on flexible substrate with 100% yield and high uniformity. The presented devices show synaptic behavior under pulse stimuli, exhibiting excitatory (inhibitory) post-synaptic current, spiking rate-dependent plasticity, and short-term to long-term memory transition. The as-realized transistors demonstrate excellent bio-like synaptic behavior and show great potential for in-hardware learning. This is demonstrated through a prototype computational e-skin, comprising event-driven sensors, synaptic transistors, and spiking neurons that bestow biological skin-like haptic sensations to a robotic hand. With associative learning, the presented computational e-skin could gradually acquire a human body–like pain reflex. The learnt behavior could be strengthened through practice. Such a peripheral nervous system–like localized learning could substantially reduce the data latency and decrease the cognitive load on the robotic platform.

INTRODUCTION

Skin, the largest organ in the human body, comprises thousands of receptors, distributed over ~18–square feet area, playing a critical role in the way we interact with the environment (*1*–*3*). It efficiently handles a large amount of tactile sensing data from all over the body and has served as the inspiration for artificial electronic skin (e-skin) (*3*–*5*). As a result, e-skin research has greatly advanced in recent years (*6*–*8*). However, existing implementations of e-skins may not be sufficient because the large amount of tactile data acquired from the skin needs to be encoded, transmitted, and preprocessed, too—similar to biological skin (*9*–*11*). It is challenging to fully emulate such functionalities owing to difficulties in terms of realizing uniformly responding electronic devices, especially synaptic devices, over large-area flexible/stretchable substrates (*11*–*16*). Now, memristor and synaptic transistor are the two promising candidates for the hardware-implemented synaptic devices (*17*–*20*). However, the fabrication complexity and notable device-to-device and cycle-to-cycle nonuniformity of memristors (such as form, set, and reset voltage), especially in a crossbar array configuration, make them challenging to use on large-area flexible substrates. Likewise, most of the currently reported work on synaptic transistor focus on a small number of devices (*21*–*24*), with almost no statistical information on the yield, uniformity, large-area weight modulation ratio, etc. Without such knowledge, the higher-level design and implementation of a synaptic transistor–based neuromorphic system are hardly possible either for online or offline learning (*25*–*28*).

Considering the surface coverage and the softness of biological skins, large-area fabrication of electronic devices on flexible/stretchable substrates is needed. To this end, printed electronics could meet these requirements in a cost-effective manner (*29*–*34*). Specifically, the printed semiconducting metal oxide nanowires (NWs) are promising candidates for the computational e-skin because of their high aspect ratio, unique electrical/optoelectrical properties, good mechanical flexibility, and compatibility with various printing technologies (*35*–*37*). However, one critical but universal challenge in printed electronics is the trade-off between spatial coverage and device uniformity—both of which are vital for robotic e-skin. This problem is more challenging for NW-based devices (i.e., transistors) because precise dimensional control and placement are difficult (*38*, *39*).

Here, we present a holistic approach for realizing highly uniform (synaptic) transistors based on printed ZnO NWs for computational e-skin. The arrays are composed of 168 devices with 100% yield, showing high DC response uniformity that surpasses (or is on par with) the state-of-the-art devices based on ZnO (Si) NW fabricated using expensive technology such as electron-beam lithography (*38*, *39*). The as-realized devices show a synaptic behavior like the biological synapse, i.e., conductance modulation based on the previous operation history, spiking rate dependency, and short-term to long-term plasticity transition. With the previously demonstrated biocompatibility in ZnO NW (*40*), the work presented here may also be promising for future integration with the biological systems.

The biomimicking synaptic behavior opens an interesting avenue for the in-hardware learning. To illustrate this, a computational e-skin prototype—composed of sensory neuron, synapse, and cuneate neuron—has been realized (see Fig. 1, A and B). The prototype fully maps the functionality of tactile neural pathway in the human body for the data encoding, transmitting, and processing; the neuron used in the pathway converts the input signal into action potentials (spikes) following biological principles, i.e., all-or-none rule, spatiotemporal summation, etc. Thanks to the bioplausibility of the as-realized system (synapses and neurons), the demonstrated e-skin shows the capability of associative learning and the further strengthening behavior by practicing, all from the in-skin hardware. This advances the previous work in e-skin (or artificial tactile pathway) by the demonstration of in-hardware associative learning and rehearsal

Bendable Electronics and Sensing Technologies (BEST) group, James Watt School of Engineering, University of Glasgow, G12 8QQ Glasgow, UK.
*Corresponding author. Email: ravinder.dahiya@glasgow.ac.uk

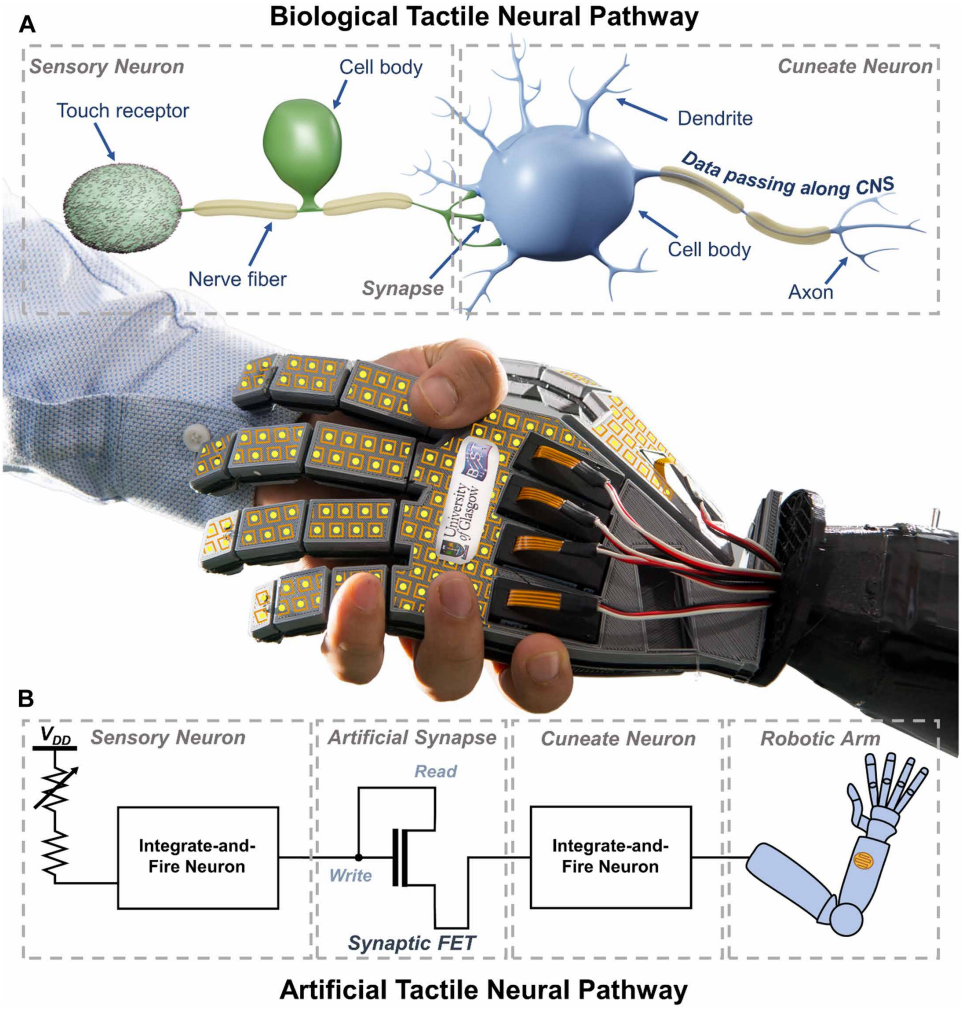

Fig. 1. The biological and artificial tactile neural pathway. (**A**) The biological tactile neural pathway. (**B**) The artificial tactile neural pathway. The connection for the artificial neural pathway is for illustration purpose only. The detailed connection is explained in Fig. 5A and fig. S10, for the case of teaching and practicing, respectively.

behavior (*13*, *19*, *41*). The large-area computational e-skin requires tactile neural pathways to cover the full body with a "many-to-many" neural connection. Such a hyperconnected network could enable a far more complicated learning behavior and built-in intelligence while substantially decreasing the data latency. To this end, the hardware implementation of large-area distributed sensing and computing requires that the as-realized synaptic transistor have a good performance, e.g., enough on/off ratio, good spatial uniformity, etc. This is important because a lack of these properties could lead to a drastic decrease of the neural network accuracy (*25*–*28*). To clarify this, a neural network simulation has also been carried out with the data from the synaptic devices, showing an average recognition rate of ~93% based on the Modified National Institute of Standards and Technology (MNIST) dataset. This is close to the full software approach (97%) and validates the potential of using the as-presented synaptic devices to realize large-scale neural network. We believe that our work paves the way for the future realization of large-area, computational e-skin and can be of interest to a broad range of readers working on neurorobotics, neuroprosthetics, smart wearables, health care monitoring, and printed/flexible electronics.

RESULTS

To fully mimic the peripheral nervous system (PNS) in the human body, hardware building blocks that can function as receptors, synapses, and neurons over a large area are prerequisites. The work presented here mainly focuses on synapses and thereafter hardware-enabled, localized learning behavior. The neuron is realized from the off-the-shelf components (see movie S1).

Hardware implementation of synaptic transistors

The bottom-gated transistors are realized by contact printing ZnO NWs from its donor to the receiver substrate, followed by photolithography, metallization, and lift-off to define the source/drain electrodes. The receiver substrate (Si with 300 nm of SiO_2) can be either a bare wafer (so that it leads to rigid devices) or a spin-coated polyimide (PI) layer (~2 μm thick). After device fabrication, the spin-on PI can be peeled off from its carrier, leading to flexible devices (see figs. S1 to S3 and Materials and Methods).

The devices realized based on the printed NWs show a 100% device yield; an ohmic output behavior (see Fig. 2, A to C) with a clear saturation at a bias voltage V_{ds} of 5 V; and a good spatial uniformity for several important device metrics such as on-state current (Fig. 2D), off-state current (Fig. 2F), on-off ratio, and threshold voltage (Fig. 2E). In general, achieving a good spatial uniformity for NW-based devices is more challenging when compared with devices based on thin-film or two-dimensional materials. This is owing to the difficulties related to good control over the material dimensions and registrations (see section S1) (*38*, *39*, *42*, *43*). In view of these challenges, the results presented here mark substantial advances because they surpass or are on par with the state-of-the-art top-gated field-effect transistors (FETs) with excellent control over diameter and registration (see table S1). Furthermore, our approach is compatible with the flexible substrate, which holds promise for applications such as large-area computational e-skin for robotics, smart wearables, health monitoring, and prosthetics. The field-effect mobility of the ZnO-based FET is estimated to be ~55 $cm^2/V \times s$. The device performance from the as-realized flexible device is robust against various mechanical bending states with almost no performance variation (fig. S4), which is a crucial prerequisite for the application in flexible electronics. This is different from previous reports where the bending of the device would lead to noticeable performance variation (*44*). We also tested the cyclic bending performance of the ZnO NW–based FETs for

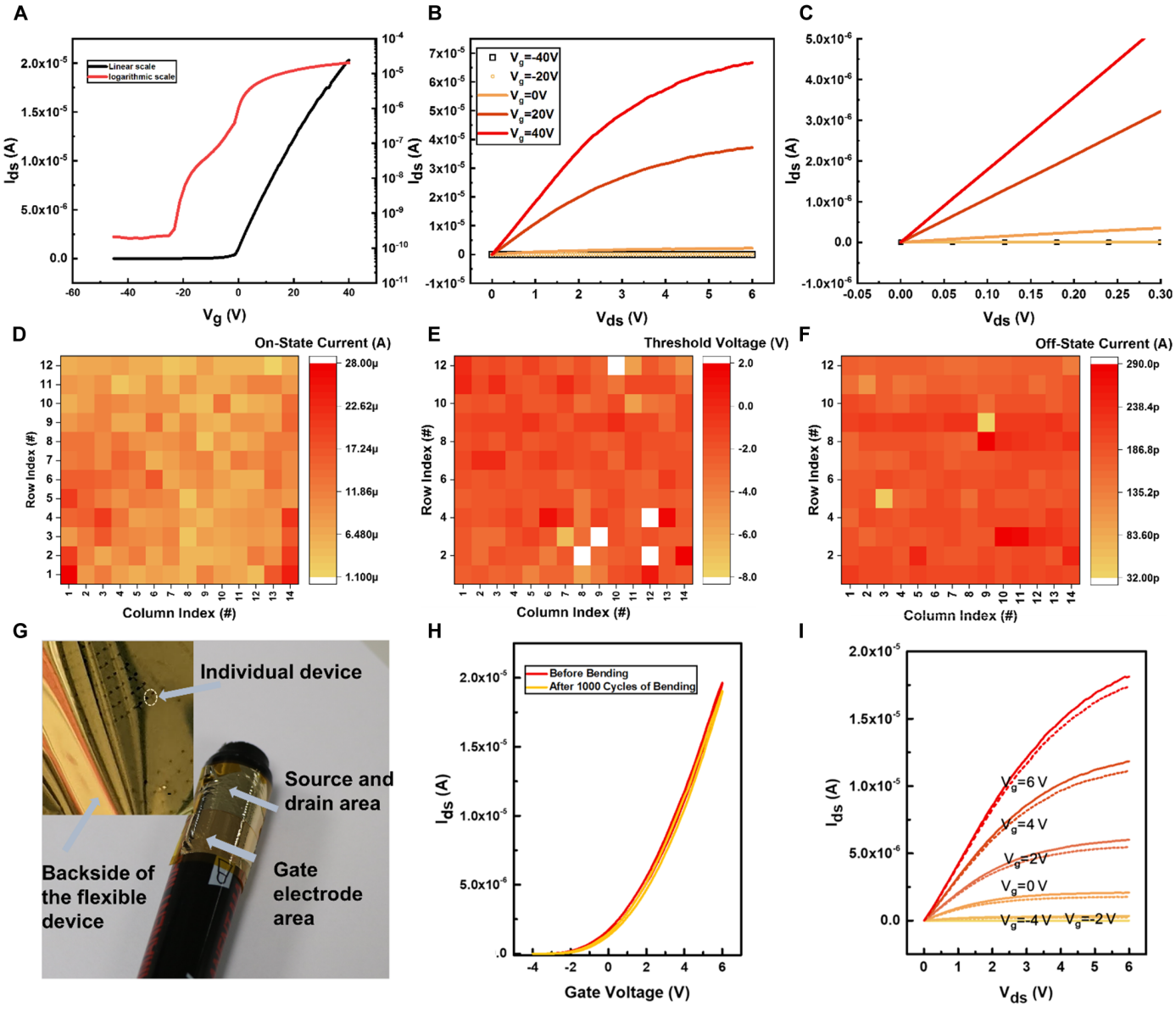

Fig. 2. The DC test of the transistors. (**A**) The transfer characteristics at a V_{ds} of 1 V. The channel length and width of the device are 10 and 220 μm, respectively. (**B** and **C**) The output characteristics at a high and low drain-to-source bias, respectively. (**D** to **F**) The spatial distribution of the on-state current, threshold voltage, and off-state current from the transistor matrix, respectively. (**G**) The photograph showing the flexibility of the devices realized on PI. (**H** and **I**) The transfer and output characteristics before and after the bending test. The transfer characteristics was measured at a V_{ds} of 6 V. Panels (A) to (F) are from tested rigid devices to prevent any probing-induced extrinsic factors. Panels (G) to (I) are from flexible device, showing that the same method can be applied to realize a flexible device matrix.

1000 cycles (at the bending radius of ~20 mm), and no notable variation in transfer and output characteristics was observed (Fig. 2, H and I). This, along with negligible shift of threshold voltage (from −2.3 to −2.1 V), confirms stability upon mechanical deformations (see fig. S4). The DC behavior of the as-realized ZnO NW FETs holds promise for realizing functional circuits, e.g., the neuron circuit required in the later study.

The transistors that we presented here emulate well the function of biological synapse: With positive (negative) pulse stimuli at the gate terminal, the drain-to-source current decreases (increases) because of the field effect. After the stimuli, the current does not go back to the original state immediately. Instead, it goes to a lower (higher) level and gradually returns to the former conductance in a quasi-exponential manner, exhibiting an inhibitory (excitatory) synaptic behavior (see Fig. 3, A and B). In the biological system, the information is passed between the neurons by emitting conductive ions (e.g., Na^+, Ca^{2+}, and Cl^-) known as neurotransmitters. Under its influence, the neuron becomes depolarized (excitatory) or hyperpolarized (inhibitory) from its resting state and gradually recovers. Similarly, the observed synaptic behavior from the presented device is attributed to the movement and trapping/detrapping of the charge carriers to those surface states under the external gate voltage bias: At the resting state ($t < 0$; Fig. 3C), the occupied surface state density and the charge carrier density in the channel are in the equilibrium

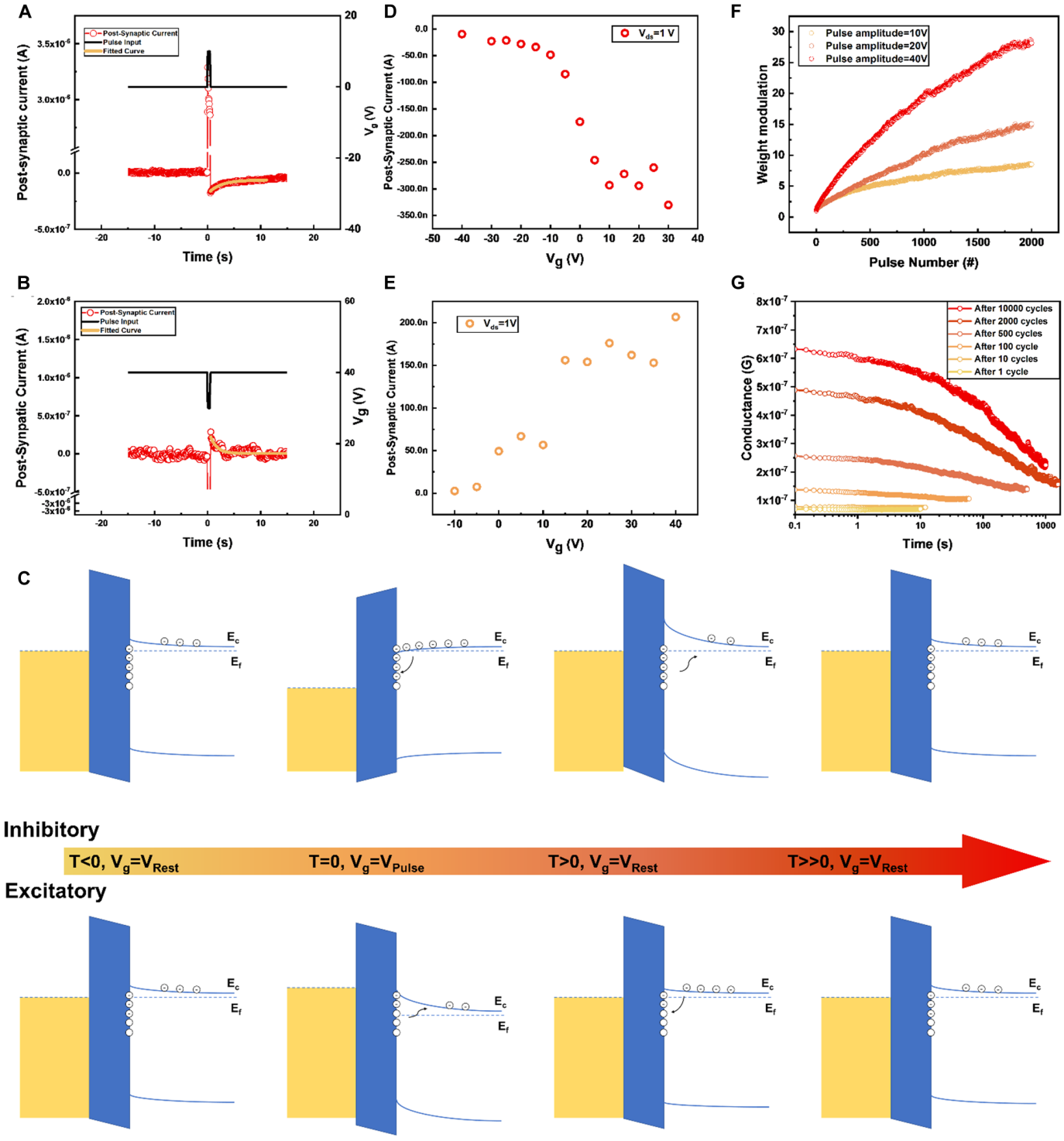

Fig. 3. The synaptic behavior of the ZnO NW–based transistor. (**A** and **B**) The inhibitory and excitatory post-synaptic current realized in transistor. (**C**) The band diagram explaining the origin of the synaptic behavior. (**D** and **E**) The dependence between the value of the post-synaptic current and the gate voltage at the resting state. (**F**) The change of modulation ratio of the conductance with respect to the number of the pulses applied to the device. The pulse width is ~300 ms, and the interval time between two neighboring stimuli is ~100 ms. (**G**) The recovery behavior of the synaptic device after certain numbers of pulse stimuli, showing a transition between STM and LTM with increased number of input pulses.

condition; once the gate voltage increases (decreases) ($t = 0$; Fig. 3C), the electron density in the channel also increases (decreases). This breaks the previous equilibrium condition, leading to more electrons trapped at the surface states (more trapped electrons escaping from the surface states). After the gate voltage returns to the resting level ($t > 0$; Fig. 3C), the carrier density in the channel becomes lower (higher) than the previous resting state level owing to a higher (lower) surface state occupancy; the unbalanced surface state occupancy gradually returns to the equilibrium condition by discharging electrons to the channel (charging electrons from the channel), leading to an inhibitory (excitatory) post-synaptic behavior ($t \gg 0$; Fig. 3C). This explanation is supported by a control experiment: After a conformable deposition of high-quality top-gate dielectric (Al_2O_3) by atomic layer deposition, the synaptic behavior vanishes (fig. S5), confirming that the synaptic behavior originated from the surface states from the ZnO NWs rather than bottom gate dielectric. The amplitude of the synaptic behavior is dependent on the base carrier density in the channel: A higher carrier density would lead to a more prominent synaptic behavior for both excitatory and inhibitory cases (Fig. 3, D and E).

It is believed that in the biological system, the increase in the amplitude and/or the frequency of applied stimuli can strengthen the synaptic behavior along with the transformation of short-term memory (STM) to long-term memory (LTM) through rehearsal (*45*, *46*). Similar behavior has been observed in our device: A change in synaptic weight from 58.3 nS to 1.64 μS (~2800%) (Fig. 3F, red curve) was observed owing to an increase in both the amplitude and the number of the pulse stimuli. After training, the conductance of the synaptic device gradually recovers to the previous state, representing the natural forgetting process. Nevertheless, with repeated stimuli or rehearsal, the retention time increases from several seconds to several minutes, which indicates a transformation from STM to LTM (Fig. 3G). We also tested the frequency dependency of synaptic behavior. The increase of pulse number and pulse frequency increases the synaptic behavior, which is a good analog of the biological behavior of paired-pulse facilitation (depression) and spiking rate–dependent plasticity (see figs. S6 and S7). Overall, the as-presented device shows a good similarity to the biological synapse, which opens the possibility for the development of the bioinspired neuromorphic system as discussed in the following section.

Tactile neural pathway capable of in-skin learning

Skin, distributed with thousands of receptors, can efficiently collect, transmit, and preprocess the tactile data in real time yet maintain an ultralow power consumption. This far surpasses most state-of-the-art robotics. Furthermore, humans exhibit great adaptability, accommodating the ever-changing environment based on the previous experience (e.g., learning). In this regard, the biological skin offers a fascinating solution for sensation and perception and acts as an excellent model for reverse engineering. Here, we present a computational e-skin prototype that fully mimics the biological, tactile neural pathway.

Similar to its biological counterpart (Fig. 1A), the artificial neural pathway consists of a (layer of) sensory neuron(s) and a (layer of) cuneate neuron(s), interconnected via synapse (Fig. 1B). The analog tactile signal is thus transduced into spikes in the first layer and further processed in the second layer. An "integrate-and-fire" neuron circuit such as the one proposed in (*47*) has been adopted to realize the functionality of the spiking neuron (see fig. S8). With respect to the arrangement of the sensory neuron, a resistive sensor [force-sensitive resistor (FSR)] is serially connected with a fixed value resistor, acting as a viable load to the neuron circuit as shown in Fig. 1B. Unlike previous approaches (*19*, *48*), this layout offers a more bioplausible spiking pattern that contains the depolarization and hyperpolarization stages (Fig. 4A), crucial for the later realization of "bio-like" learning in the e-skin. The output spiking pattern from the sensory neuron can be tuned by the value of the built-in

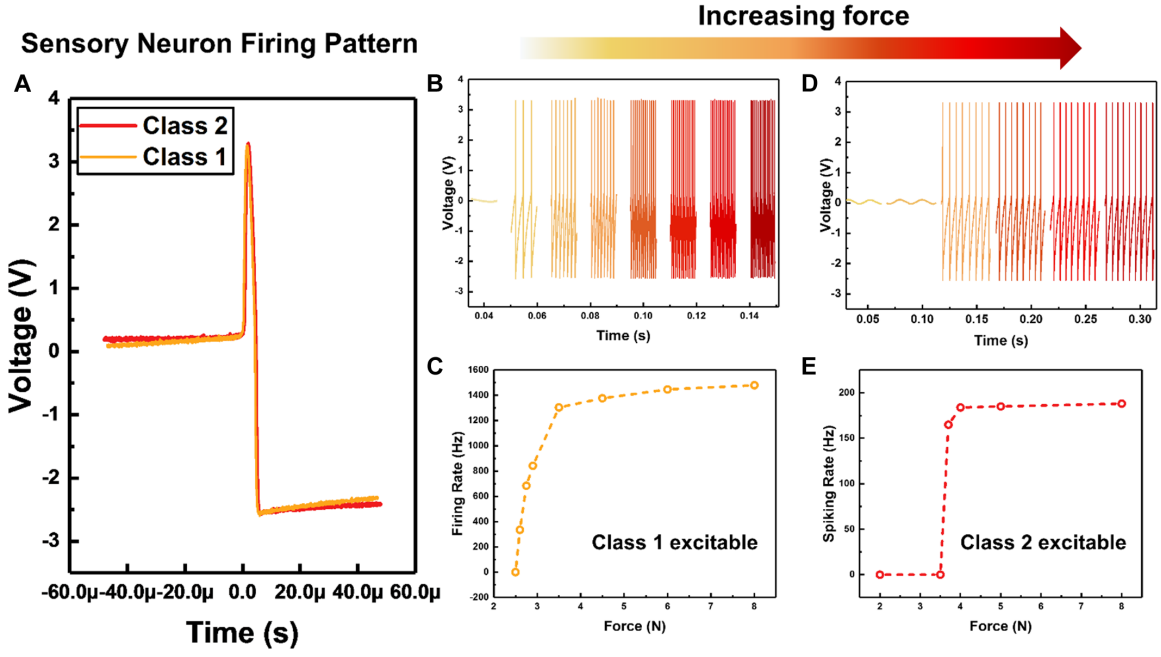

Fig. 4. The firing pattern of the sensory neuron. (**A**) The single spike from the sensory neuron. (**B** and **C**) The change of the firing rate with respect to the applied force for the class 1 excitable neuron. (**D** and **E**) The change of the firing rate with respect to the applied force for the class 2 excitable neuron.

resistor. For example, using the FSR with a 1-megohm (or lower) resistor, the sensory neuron circuit exhibits a class 1 excitable behavior (*49*); that is, the firing rate positively related to the applied stimuli (Fig. 4, B and C). Meanwhile, the FSR connected with a resistor of 10 megohms (or higher) would lead to a class 2 excitable behavior (spiking rate independent of the incoming stimuli if it is higher than the threshold, Fig. 4, D and E) (*49*). It should be noted that both designs offer event-driven sensing, drastically reducing the latency of the tactile data that need to be fed into the neural pathway. In this work, we adopt the latter design to act as the artificial nociceptor and further use it to emulate the pain reflex observed in biology.

A hardware-implemented neural system opens the possibility of realizing bio-like learning behavior. In the biological neural system, the synaptic weight is determined by a pair of pre- and post-neuron spiking signals, i.e., spiking time–dependent plasticity and burst time–dependent plasticity (*50*, *51*). A pair of synchronized spikes changes the synaptic weight according to their relative timing and thus leads to the learning behavior. By contrast, a standalone incoming signal should not affect the synaptic weight much because, in this scenario, the pre- and post-spiking signals are regarded as highly unsynchronized. In biological view, this opens room for the neural system to react only to those conditions they are supposed to or trained to. In the presented artificial neural pathway, this is demonstrated by the presented synaptic device along with the spiking neuron circuit capable of delivering the highly bioplausible action potentials. The synaptic device passes the spiking signal to the next level (read) and changes its own weight under the pre- and post-spiking pair (write); each pressing of the sensor should cover at least one write and one read process (Fig. 5A). The switching of the read and write could be achieved in various manners, for example, by using a global clock signal. In this regard, a clock of 1000 Hz should be enough for tactile sensing because the average tactile reaction time observed in the human body is ~200 ms (*52*), 200 times longer than a clock cycle. The detailed connections of each node of the synaptic transistor (for the read and write modes) are summarized in Fig. 5A. It should also be noted that to achieve more effective training, the sensory signal used in the write mode is amplified by ~4 times (Fig. 5B). This could be potentially avoided by using a dielectric that is four times thinner; thus, the amplitude of the sensory spiking could stay the same for both modes.

The untrained scenario of the tactile neural pathway is shown in Fig. 5C. With only the sensory spiking, the weight of the synaptic device remains almost the same; thus, the second-order neuron stays silent. This is owing to the use of the biological spiking patterns from the sensory neuron: As discussed in Fig. 3 (A and B), the positive (negative) electrical stimulus leads to an inhibitory (excitatory) behavior to the synaptic device; the coexistence of the electrical stimulus in both direction within one pulse would then open room for the synaptic weight to stay unchanged. In this scenario, the synaptic device cannot be trained by a single pulse from the sensory neuron because a pre-spiking signal alone leads to no post-spiking signal under a low-weight synaptic connection, and this failure of excitation remains in loop. From a functionality point of view, this represents an unconfigured computational e-skin, similar to those patients who suffer from hypoesthesia and partially lost their somatosensation, which stops them from responding to certain types of stimuli (e.g., pain) in a certain part of their body because of the loss of the previous synaptic weight.

Clinically, those patients may regain the sensation by passive sensory training using peripheral electrical stimulation, which externally modulates the synaptic plasticity. Despite that the optimal stimulation frequency and waveform for this purpose are still ambiguous, it is generally accepted that a longer electrical stimulation leads to stronger plasticity modulation (*53*). Similarly, the presented computational e-skin could be configured to react to certain behavior through a teacher signal to evoke the second-order neuron's firing through associative learning. The required teacher signal was used right at the time of the touch (see Fig. 5B), which excites the second-order neuron and trained the synapse. As shown in Fig. 5D, the weight of the synaptic transistor was facilitated to ~50 nA after the associative learning, and such an effect was not disturbed by the stimulation of the sensors (Fig. 5D). Owing to the excitatory of the synapse, the second-order neuron receives a stronger input that is larger than its firing threshold, thus changing from the nonfiring to the firing condition (Fig. 5E). Furthermore, just like the clinical observation, the longer the teacher sensory signal pair was applied, the stronger the associated learning would become (see movies S2 and S3 and fig. S9 showing STM and LTM after associative learning). After teaching, the learnt behavior is strengthened/retained if it is practiced regularly so that the pre-neuron spiking would evoke a post-neuron spiking, and such a synchronized spiking pair could rehearse the associated behavior on time (see fig. S10 and movie S4 for the feedback behavior of the neural pathway). After training, the second-order neuron fires an action potential whenever there is an over-threshold stimulus on the sensor in the neural pathway; by contrast, without training (or without pressing), the second-order neuron remains in the subthreshold oscillation (or off state) (Fig. 5E). Such in-skin learning is attractive because this could drastically reduce the data latency and minimize the cognitive load of the central control unit of the robot. This is especially important for tactile sensing because large numbers of tactile receptors (mechano, thermal, and pain) are distributed all over the skin, and it is challenging to carry large-scale tactile data from PNS to central nervous system (CNS). The methodology presented here mimics the biological process in tactile sensation and perception, where the tactile information is locally preprocessed in PNS before transferring (*9*, *10*), complementing the functionality of the CNS. In the work presented here, the neural signal from the tactile pathway was fed into a robotic arm (from Universal Robots). After associative learning, the robotic hand acquires the pain reflex, like the one that the human body has (see Fig. 5F and movies S1 and S5). Compared with the previous demonstration of the artificial tactile pathway (*13*, *19*, *41*), the work presented here fully mimics the neurological principles, thus showing the capability of "bio-like" learning directly on the hardware level.

Toward large-area, multifuncitonal e-skin

Skin contains many multimodal sensors, with different threshold and receptive fields. Along with the associated neurons and synapses, it forms a large-area neural system covering the whole body. It is necessary to extend the above-presented "one-to-one" biological neuron pathway into a many-to-many multilayer neural network capable of doing cognitive tasks using various methods including supervised, unsupervised, and reinforcement learning (see fig. S11 along with the detailed discussion in the section S8). One critical step toward this is the realization of large-area synaptic devices. In practice, hardware-implemented synapses have several limitations such as finite weight modulation ratio with discrete values, spatial nonuniformity,

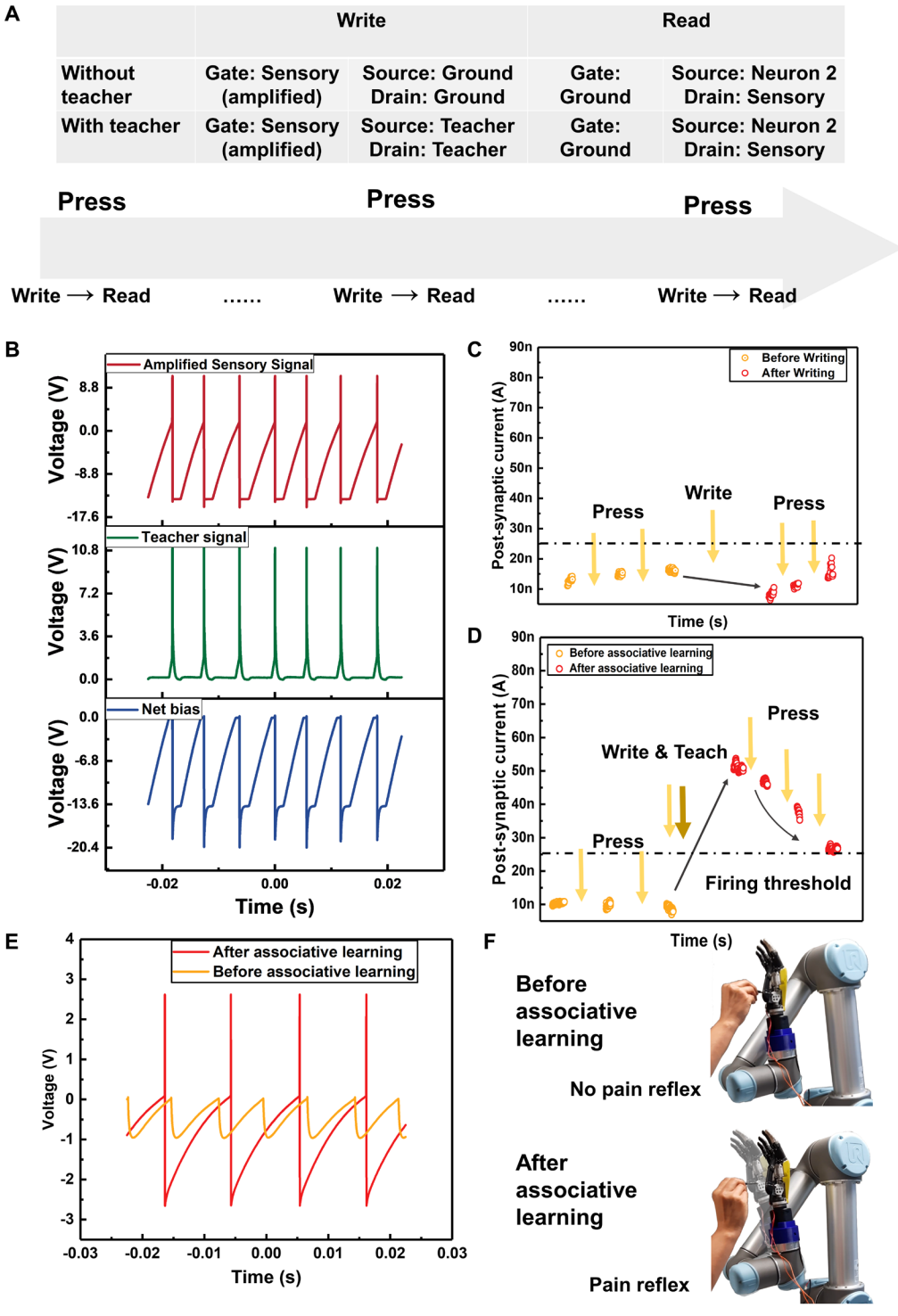

Fig. 5. The demonstration of the artificial tactile neural pathway capable of "in-skin" learning. (**A**) The detailed operation scheme for the tactile neural pathway. (**B**) The spiking signal used for the writing stage. (**C**) Without a teacher signal, the computational e-skin cannot learn, so it does not respond to applied force. (**D**) With a teacher signal, the computational e-skin can realize localized learning. The threshold shown in the figure is for illustration purpose only. (**E**) The firing pattern of the cuneate neuron (second-order neuron) before and after associative learning, with the applied force on the sensor. (**F**) Images showing the acquired pain reflex after associative learning right on the skin level.

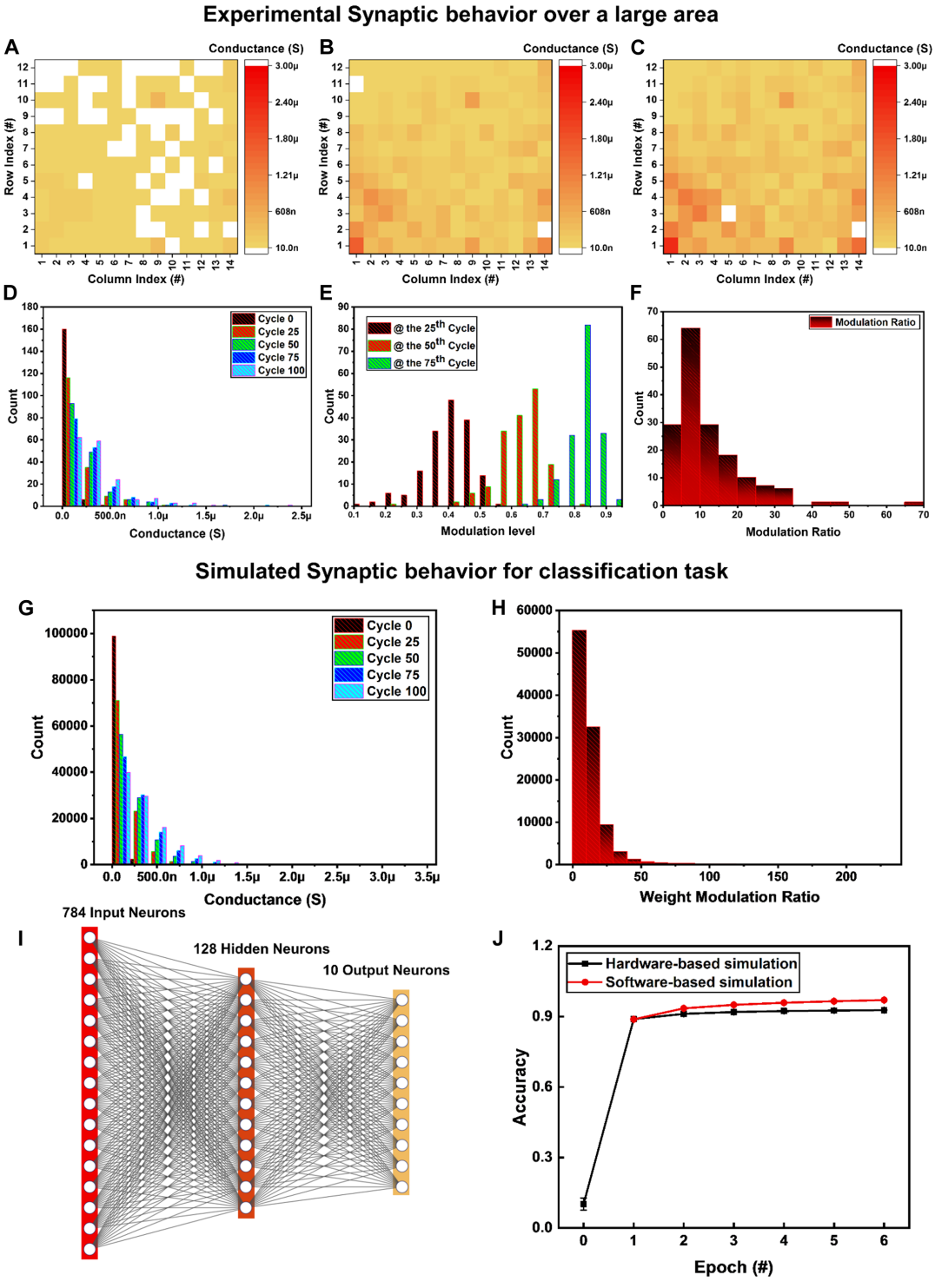

Fig. 6. The large-area synaptic responses and the neural network simulation. The synaptic response over the entire matrix and the neural network simulation. (**A** to **C**) The spatial distribution of the conductance of the pixel at the 0th, 50th, and 100th cycle, respectively. (**D** to **F**) The distribution of the conductance, modulation level, and modulation ratio, respectively. The modulation level at the *i*th cycle is defined as $(G_i - G_0)/(G_{100} - G_0)$. (**G** and **H**) The distribution of the conductance and weight modulation level from the extrapolated hardware dataset. The dataset is composed of 101,771 groups of conductance information. Within each group, the conductance level is changed from cycle 0 to cycle 100. (**I**) The three-layer feedforward type neural network trained for the handwritten digits classification. The training was done using the MNIST dataset. (**J**) The comparison between the software-based training and hardware-based training.

and the device yield problem. Although the neural network is naturally resilient to some of these limitations, studies have shown that a high-weight modulation range for the synapse with decent uniformity is necessary to obtain a good network accuracy (*25*–*28*). This has posed the requirement for the hardware-implemented synaptic devices. Here, as a step toward the large-area computational e-skin, we systematically evaluated the synaptic behavior from the transistors. For all the devices, a series of 100 excitatory pulses has been used and the conductance was measured. The as-realized devices show a good weight modulation ratio (>500%) for most of the devices (>80%) with fine modulation steps, which is beneficial for the neuromorphic system realization (Fig. 6, A, B, C, and F) (*25*–*28*). The conductance of the synaptic devices with respect to the input pulse cycle is presented in Fig. 6 (A to C); 100% of the as-realized devices show the synaptic behavior with a cell-to-cell variation (σ/μ) of ~96 and ~ 133% at the 100th and 0th cycle, respectively (Fig. 6D), larger than the nonuniformity in the DC response. To further verify the applicability of the as-realized devices for neuromorphic computing, we used the weight data from the realized synaptic devices to simulate a three-layer feedforward neural network. On the basis of the spatial (14 by 12 devices) and temporal (0 to 100 cycles) weight distribution from 168 devices, we have extrapolated to obtain a dataset of 101,771 groups (101 discrete weight value for each group) by assuming that both datasets follow the same distribution (see Fig. 6, D, F, G, and H, and figs. S12 and S13). The weights constructed a "hardware library" and trained to recognize handwritten digits by using the MNIST dataset (Fig. 6I). Such a strategy enables us to evaluate the quality of synaptic behavior from all devices instead of a single device. For comparison, we also simulated the full analog weights to represent the software approach. The neural network simulation has been repeated 10 times, and the average accuracy is presented here. As can be seen in Fig. 6J, the recognition accuracy based on the hardware simulation is ~93% at the sixth epoch, which is only 4% less than the software-based simulation. This indicates a good synaptic performance from the transistors and hence a good indication for using it to realize large-scale neural network. By contrast, with a decreased weight modulation ratio or high nonuniformity from the synapses, the constructed neural networks were shown to have a notably lower recognition accuracy (*27*).

DISCUSSION

We have realized large-area, uniform, printed synaptic transistors and further use them to realize a computational e-skin. The e-skin mimics the biological tactile neural pathway and offers an in-skin computing (learning) capability. Such a distributed learning through hardware holds great potential for the next-generation robots because it will drastically decrease the cognitive load on their central control units. There are also several limitations from the work presented here: Only the synaptic transistor in the neural pathway is realized on the flexible substrate. Also, in the computational e-skin prototype, we demonstrated a one-to-one neuron control with learning capability. Further extending this work toward all-printed, flexible artificial neural pathway in a many-to-many neural network fashion would enable a fully flexible e-skin with much higher built-in intelligence. Nevertheless, we believe that this work, as a first step, paves the way for the future realization of large-area, multifunctional, and fully printed computational e-skin.

MATERIALS AND METHODS

NW synthesis

The ZnO NW was synthesized by chemical vapor transport method using a tube furnace. Before synthesis, the substrate (Si) was treated by poly-L-lysine solution 0.1% (w/v) in H_2O for 20 s, followed by Au nanoparticle (diameter of 80 nm) suspension treatment for 40 s. The substrate was then rinsed with reverse-osmosis water and cleaned by a mild oxygen plasma (80 W) for 200 s. The Si substrate with Au nanoparticles was then loaded into the furnace for ZnO NW synthesis with a mixture of 0.5 g of ZnO powder and 0.5 g of graphite powder as the source material. The placement of the substrate with respect to the source can be found in the Supplementary Materials. Such placement has been found to offer a good spatial uniformity. The synthesis was carried out at 880°C for 2 hours, with the Ar acting as the carrier gas of ~1500 standard cubic centimeters per minute.

Receiver substrate preparation

Si substrate with a 300-nm thermal oxide layer was used as the rigid substrate. Before NW printing, the substrate was deposited with 70-nm SiN_x for surface passivation with ICP 380 from Oxford Instrument. The flexible receiver substrate was prepared by spin-coating PI layer on top of the Si (with a 300-nm oxide layer) carrier wafer. The PI was spin-coated at 500 rpm for 5 s and 2000 rpm for 60 s. The spin coating was carried out twice, with 140°C soft baking for 5 min between each coating. The sample was ready for use after a full curing at 250°C for 2 hours. After all of the fabrication process, the PI layer can be peeled off from the carrier wafer, leading to a flexible film with as-realized devices.

Contact printing

The contact printing process was carried out using an automated, homemade setup (*54*). The setup can deliver a close-loop control of the printing process in terms of the contact pressure, sliding speed, sliding stroke, etc. The conformable contact was guaranteed by a specifically designed self-leveling system. The printing process was monitored by two micro cameras from two perpendicular directions. The printing process together with the automated setup was explained in our publication (*54*).

Device fabrication

After printing, the sample was baked on a hotplate at 160° to 180°C for 5 min. Without such a baking process, the NW would be substantially disturbed in the following lithography process because of the weak van der Waals contact between the NWs and the underlying substrate. The sample was then spin-coated with LOR 10A at 6000 rpm for 30 s, baked at 150°C for 2 min, then spin-coated with S1818 at 4000 rpm for 30 s, and baked at 115°C for 3 min. The exposure was carried out by Mask Aligner 6 for a duration of 6 s. The sample was then developed in MF319 for 85 s, followed by metal deposition (8-nm Ti and 50-nm Au) and lift-off. The lift-off process was carried out in MICROPOSIT remover 1165 for 30 min under the 50°C water bath. Such a long-time water bath could effectively remove most of the printed NWs, unless they are buried under the source and drain contacts.

Device measurement

The device was measured in the ambient condition with the source/measure unit B2912A from Keysight. Because of the resolution of our measurement system for the pulse test, we kept a constant white light excitation for all the devices to see the synaptic behavior. The

devices are measured all together at the same condition to minimize those nonuniform extrinsic factors. For synaptic measurement, pulse voltage signals with positive and negative polarities were applied to gate terminal, and drain-to-source current was measured, keeping the drain voltage constant. The drain-to-source current measured after pulse signal is referred as post-synaptic current.

Statistical analysis

The statistical analysis performed in the manuscript—including the distribution identification, normality test, and random data generation—was carried out using Minitab or MATLAB.

Neuron circuit implementation

The neuron circuit was implemented by using two complementary metal-oxide semiconductor dual complementary pair integrated circuits (CD4007). Its circuit diagram is shown in the Supplementary Materials.

Robot experiment

A Nucleo board was used to sample and detect the spiking signal. Whenever a continuous spiking signal was detected, a control command was sent to trigger the UR5 arm. The threshold needs to be chosen properly so that, on one hand, it would not be triggered by any noise signal, and on the other hand, it should lead to a prompt reaction. The General-Purpose Input/Output (GPIO) pin was left on high for 50 ms to ensure detection by the UR5 arm.

Neural network simulation

We evaluated the uniformity of the hardware synaptic behavior in the framework of supervised learning in neural network. The three-layer feedforward neural network was trained using the TensorFlow library for Python 3.7. The training was carried out with the loss function of "sparse categorical crossentropy" and the activation function of hyperbolic tangent function (Tanh). For hardware-based simulation, the initial weight of the entire neural network was assigned to be the conductance data from the 0th cycle but in a random manner. The computation of gradients was carried out by backpropagation method but at the hardware constrain condition. This was mimicked by choosing the closest weights from the extended hardware dataset (Fig. 6G) at each epoch with respect to the software-training value and used this for further update. For simplicity, the hardware weights are all scaled by a factor of 10^6.

SUPPLEMENTARY MATERIALS

www.science.org/doi/10.1126/scirobotics.abl7286
Figs. S1 to S13
Table S1
Movies S1 to S5
References (*55*–*70*)

REFERENCES AND NOTES

1. P. Escobedo, M. Ntagios, D. Shakthivel, W. T. Navaraj, R. Dahiya, Energy generating electronic skin with intrinsic tactile sensing without touch sensors. *IEEE Trans. Robot.* **37**, 683–690 (2021).
2. S. Coren, L. M. Ward, J. T. Enns, *Sensation and Perception* (John Wiley & Sons Hoboken, 2004).
3. R. S. Dahiya, G. Metta, M. Valle, G. Sandini, Tactile sensing—From humans to humanoids. *IEEE Trans. Robot.* **26**, 1–20 (2010).
4. R. Mukherjee, P. Ganguly, R. Dahiya, Bioinspired distributed energy in robotics and enabling technologies. *Adv. Intell. Syst.* , 2100036 (2021).
5. J. C. Yang, J. Mun, S. Y. Kwon, S. Park, Z. Bao, S. Park, Electronic skin: Recent progress and future prospects for skin-attachable devices for health monitoring, robotics, and prosthetics. *Adv. Mater.* **31**, 1904765 (2019).
6. R. S. Dahiya, M. Valle, *Robotic Tactile Sensing: Technologies and System* (Springer Science & Business Media, 2013).
7. C. M. Boutry, M. Negre, M. Jorda, O. Vardoulis, A. Chortos, O. Khatib, Z. Bao, A hierarchically patterned, bioinspired e-skin able to detect the direction of applied pressure for robotics. *Sci. Robot.* **3**, eaau6914 (2018).
8. T. Someya, M. Amagai, Toward a new generation of smart skins. *Nat. Biotechnol.* **37**, 382–388 (2019).
9. J. A. Pruszynski, R. S. Johansson, Edge-orientation processing in first-order tactile neurons. *Nat. Neurosci.* **17**, 1404–1409 (2014).
10. R. S. Johansson, J. R. Flanagan, Coding and use of tactile signals from the fingertips in object manipulation tasks. *Nat. Rev. Neurosci.* **10**, 345–359 (2009).
11. R. Dahiya, N. Yogeswaran, F. Liu, L. Manjakkal, E. Burdet, V. Hayward, H. Jorntell, Large-area soft e-skin: The challenges beyond sensor designs. *Proc. IEEE* **107**, 2016–2033 (2019).
12. M. A. Zidan, J. P. Strachan, W. D. Lu, The future of electronics based on memristive systems. *Nat. Electron.* **1**, 22–29 (2018).
13. H. Tan, Q. Tao, I. Pande, S. Majumdar, F. Liu, Y. Zhou, P. O. Å. Persson, J. Rosen, S. van Dijken, Tactile sensory coding and learning with bio-inspired optoelectronic spiking afferent nerves. *Nat. Commun.* **11**, 1369 (2020).
14. R. A. John, N. Tiwari, M. I. B. Patdillah, M. R. Kulkarni, N. Tiwari, J. Basu, S. K. Bose, Ankit, C. J. Yu, A. Nirmal, S. K. Vishwanath, C. Bartolozzi, A. Basu, N. Mathews, Self healable neuromorphic memtransistor elements for decentralized sensory signal processing in robotics. *Nat. Commun.* **11**, 4030 (2020).
15. W. W. Lee, Y. J. Tan, H. Yao, S. Li, H. H. See, M. Hon, K. A. Ng, B. Xiong, J. S. Ho, B. C. K. Tee, A neuro-inspired artificial peripheral nervous system for scalable electronic skins. *Sci. Robot.* **4**, eaax2198 (2019).
16. M. Soni, R. Dahiya, Soft eSkin: Distributed touch sensing with harmonized energy and computing. *Philos. Trans. R. Soc. A* **378**, 20190156 (2020).
17. C. Li, D. Belkin, Y. Li, P. Yan, M. Hu, N. Ge, H. Jiang, E. Montgomery, P. Lin, Z. Wang, W. Song, J. P. Strachan, M. Barnell, Q. Wu, R. S. Williams, J. J. Yang, Q. Xia, Efficient and self-adaptive in-situ learning in multilayer memristor neural networks. *Nat. Commun.* **9**, 2385 (2018).
18. M. Prezioso, F. Merrikh-Bayat, B. D. Hoskins, G. C. Adam, K. K. Likharev, D. B. Strukov, Training and operation of an integrated neuromorphic network based on metal-oxide memristors. *Nature* **521**, 61–64 (2015).
19. Y. Kim, A. Chortos, W. Xu, Y. Liu, J. Y. Oh, D. Son, J. Kang, A. M. Foudeh, C. Zhu, Y. Lee, S. Niu, J. Liu, R. Pfattner, Z. Bao, T.-W. Lee, A bioinspired flexible organic artificial afferent nerve. *Science* **360**, 998–1003 (2018).
20. E. Baek, N. R. Das, C. V. Cannistraci, T. Rim, G. S. C. Bermúdez, K. Nych, H. Cho, K. Kim, C.-K. Baek, D. Makarov, R. Tetzlaff, L. Chua, L. Baraban, G. Cuniberti, Intrinsic plasticity of silicon nanowire neurotransistors for dynamic memory and learning functions. *Nat. Electron.* **3**, 398–408 (2020).
21. H. Wan, Y. Cao, L.-W. Lo, J. Zhao, N. Sepúlveda, C. Wang, Flexible carbon nanotube synaptic transistor for neurological electronic skin applications. *ACS Nano* **14**, 10402–10412 (2020).
22. H. Shim, K. Sim, F. Ershad, P. Yang, A. Thukral, Z. Rao, H.-J. Kim, Y. Liu, X. Wang, G. Gu, L. Gao, X. Wang, Y. Chai, C. Yu, Stretchable elastic synaptic transistors for neurologically integrated soft engineering systems. *Sci. Adv.* **5**, eaax4961 (2019).
23. C. S. Yang, D. S. Shang, N. Liu, G. Shi, X. Shen, R. C. Yu, Y. Q. Li, Y. Sun, A synaptic transistor based on quasi-2D molybdenum oxide. *Adv. Mater.* **29**, 1700906 (2017).
24. Q. Lai, L. Zhang, Z. Li, W. F. Stickle, R. S. Williams, Y. Chen, Ionic/electronic hybrid materials integrated in a synaptic transistor with signal processing and learning functions. *Adv. Mater.* **22**, 2448–2453 (2010).
25. S. Park, A. Sheri, J. Kim, J. Noh, J. Jang, M. Jeon, B. Lee, B. R. Lee, B. H. Lee, H. Hwang, Neuromorphic speech systems using advanced ReRAM-based synapse, in *2013 IEEE International Electron Devices Meeting* (IEEE, 2013), pp. 25.6.1–25.6.4.
26. G. W. Burr, R. M. Shelby, S. Sidler, C. di Nolfo, J. Jang, I. Boybat, R. S. Shenoy, P. Narayanan, K. Virwani, E. U. Giacometti, B. N. Kurdi, H. Hwang, Experimental demonstration and tolerancing of a large-scale neural network (165 000 synapses) using phase-change memory as the synaptic weight element. *IEEE Trans. Electron Devices* **62**, 3498–3507 (2015).
27. S. Kim, M. Lim, Y. Kim, H.-D. Kim, S.-J. Choi, Impact of synaptic device variations on pattern recognition accuracy in a hardware neural network. *Sci. Rep.* **8**, 2638 (2018).
28. S. Yu, P. -Y. Chen, Y. Cao, L. Xia, Y. Wang, H. Wu, Scaling-up resistive synaptic arrays for neuro-inspired architecture: Challenges and prospect, in *2015 IEEE International Electron Devices Meeting (IEDM)* (IEEE, 2015), pp. 17.3.1–17.3.4.
29. J. A. Rogers, T. Someya, Y. Huang, Materials and mechanics for stretchable electronics. *Science* **327**, 1603–1607 (2010).
30. C. Jiang, H. W. Choi, X. Cheng, H. Ma, D. Hasko, A. Nathan, Printed subthreshold organic transistors operating at high gain and ultralow power. *Science* **363**, 719–723 (2019).

31. K. Takei, T. Takahashi, J. C. Ho, H. Ko, A. G. Gillies, P. W. Leu, R. S. Fearing, A. Javey, Nanowire active-matrix circuitry for low-voltage macroscale artificial skin. *Nat. Mater.* **9**, 821–826 (2010).
32. M. L. Hammock, A. Chortos, B. C.-K. Tee, J. B.-H. Tok, Z. Bao, 25th anniversary article: The evolution of electronic skin (E-Skin): A brief history, design considerations, and recent progress. *Adv. Mater.* **25**, 5997–6038 (2013).
33. A. Zumeit, A. S. Dahiya, A. Christou, D. Shakthivel, R. Dahiya, Direct roll transfer printed silicon nanoribbon arrays based high-performance flexible electronics. *npj Flex. Electron.* **5**, 18 (2021).
34. A. S. Dahiya, Y. Kumaresan, D. Shakthivel, A. Zumeit, A. Christou, R. Dahiya, High-performance printed electronics based on inorganic semiconducting nano to chip scale structures. *Nano Converg.* **7**, 33 (2020).
35. Z. Fan, J. C. Ho, Z. A. Jacobson, R. Yerushalmi, R. L. Alley, H. Razavi, A. Javey, Wafer-scale assembly of highly ordered semiconductor nanowire arrays by contact printing. *Nano Lett.* **8**, 20–25 (2008).
36. C. García Núñez, F. Liu, W. T. Navaraj, A. Christou, D. Shakthivel, R. Dahiya, Heterogeneous integration of contact-printed semiconductor nanowires for high-performance devices on large areas. *Microsyst. Nanoeng.* **4**, 22 (2018).
37. T. Takahashi, K. Takei, E. Adabi, Z. Fan, A. M. Niknejad, A. Javey, Parallel array InAs nanowire transistors for mechanically bendable, ultrahigh frequency electronics. *ACS Nano* **4**, 5855–5860 (2010).
38. M. Schvartzman, D. Tsivion, D. Mahalu, O. Raslin, E. Joselevich, Self-integration of nanowires into circuits via guided growth. *Proc. Natl. Acad. Sci. U.S.A.* **110**, 15195–15200 (2013).
39. J. Yao, H. Yan, C. M. Lieber, A nanoscale combing technique for the large-scale assembly of highly aligned nanowires. *Nat. Nanotechnol.* **8**, 329–335 (2013).
40. Z. Li, R. Yang, M. Yu, F. Bai, C. Li, Z. L. Wang, Cellular level biocompatibility and biosafety of ZnO nanowires. *J. Phys. Chem. C* **112**, 20114–20117 (2008).
41. S. Chun, J.-S. Kim, Y. Yoo, Y. Choi, S. J. Jung, D. Jang, G. Lee, K.-I. Song, K. S. Nam, I. Youn, D. Son, C. Pang, Y. Jeong, H. Jung, Y.-J. Kim, B.-D. Choi, J. Kim, S.-P. Kim, W. Park, S. Park, An artificial neural tactile sensing system. *Nat. Electron.* **4**, 429–438 (2021).
42. A. I. Hochbaum, R. Fan, R. He, P. Yang, Controlled growth of Si nanowire arrays for device integration. *Nano Lett.* **5**, 457–460 (2005).
43. M. Collet, S. Salomon, N. Y. Klein, F. Seichepine, C. Vieu, L. Nicu, G. Larrieu, Large-scale assembly of single nanowires through capillary-assisted dielectrophoresis. *Adv. Mater.* **27**, 1268–1273 (2015).
44. S.-S. Kwon, W.-K. Hong, G. Jo, J. Maeng, T.-W. Kim, S. Song, T. Lee, Piezoelectric effect on the electronic transport characteristics of ZnO nanowire field-effect transistors on bent flexible substrates. *Adv. Mater.* **20**, 4557–4562 (2008).
45. T. Ohno, T. Hasegawa, T. Tsuruoka, K. Terabe, J. K. Gimzewski, M. Aono, Short-term plasticity and long-term potentiation mimicked in single inorganic synapses. *Nat. Mater.* **10**, 591–595 (2011).
46. B. H. Ross, *The Psychology of Learning and Motivation: Advances in Research and Theory* (Academic Press, 2009).
47. I. Sourikopoulos, S. Hedayat, C. Loyez, F. Danneville, V. Hoel, E. Mercier, A. Cappy, A 4-fJ/spike artificial neuron in 65 nm CMOS technology. *Front. Neurosci.* **11**, 123 (2017).
48. B. C.-K. Tee, A. Chortos, A. Berndt, A. K. Nguyen, A. Tom, A. McGuire, Z. C. Lin, K. Tien, W. G. Bae, H. Wang, P. Mei, H. H. Chou, B. Cui, K. Deisseroth, T. N. Ng, Z. Bao, A skin-inspired organic digital mechanoreceptor. *Science* **350**, 313–316 (2015).
49. E. M. Izhikevich, Which model to use for cortical spiking neurons? *IEEE Trans. Neural Netw.* **15**, 1063–1070 (2004).
50. H. Z. Shouval, S. S.-H. Wang, G. M. Wittenberg, Spike timing dependent plasticity: A consequence of more fundamental learning rules. *Front. Comput. Neurosci.* **4**, 19 (2010).
51. D. A. Butts, P. O. Kanold, The applicability of spike time dependent plasticity to development. *Front. Synaptic Neurosci.* **2**, 30 (2010).
52. J. Kim, E. Francisco, J. Holden, R. Lensch, B. Kirsch, R. Dennis, M. Tommerdahl, Visual vs. tactile reaction testing demonstrates problems with online cognitive testing. *J. Sci. Med.* **2**, 1–7 (2020).
53. L. S. Chipchase, S. M. Schabrun, P. W. Hodges, Peripheral electrical stimulation to induce cortical plasticity: A systematic review of stimulus parameters. *Clin. Neurophysiol. Pract.* **122**, 456–463 (2011).
54. A. Christou, F. Liu, R. Dahiya, Highly controlled automated system for large-area directional printing of quasi-1D nanostructures. *Microsyst. Nanoeng* **7**, 1–12 (2021).
55. Y. Liang, M. Xiao, D. Wu, Y. Lin, L. Liu, J. He, G. Zhang, L. M. Peng, Z. Zhang, Wafer-scale uniform carbon nanotube transistors for ultrasensitive and label-free detection of disease biomarkers. *ACS Nano* **14**, 8866–8874 (2020).
56. L. Liu, J. Han, L. Xu, J. Zhou, C. Zhao, S. Ding, H. Shi, M. Xiao, L. Ding, Z. Ma, C. Jin, Z. Zhang, L. M. Peng, Aligned, high-density semiconducting carbon nanotube arrays for high-performance electronics. *Science* **368**, 850–856 (2020).
57. D. C. Rubin, A. E. Wenzel, One hundred years of forgetting: A quantitative description of retention. *Psychol. Rev.* **103**, 734–760 (1996).
58. G. R. Poe, Sleep is for forgetting. *J. Neurosci.* **37**, 464–473 (2017).
59. C. W. Eurich, H. Schwegler, Coarse coding: Calculation of the resolution achieved by a population of large receptive field neurons. *Biol. Cybern.* **76**, 357–363 (1997).
60. D. R. Lesniak, K. L. Marshall, S. A. Wellnitz, B. A. Jenkins, Y. Baba, M. N. Rasband, G. J. Gerling, E. A. Lumpkin, Computation identifies structural features that govern neuronal firing properties in slowly adapting touch receptors. *eLife* **3**, e01488 (2014).
61. F. Vega-Bermudez, K. Johnson, SA1 and RA receptive fields, response variability, and population responses mapped with a probe array. *J. Neurophysiol.* **81**, 2701–2710 (1999).
62. H. P. Saal, B. P. Delhaye, B. C. Rayhaun, S. J. Bensmaia, Simulating tactile signals from the whole hand with millisecond precision. *Proc. Natl. Acad. Sci. U.S.A.* **114**, E5693–E5702 (2017).
63. V. Hayward, Is there a 'plenhaptic'function? *Philos. Trans. R. Soc. Lond. B Biol. Sci.* **366**, 3115–3122 (2011).
64. S. N. Haber, B. Knutson, The reward circuit: Linking primate anatomy and human imaging. *Neuropsychopharmacology* **35**, 4–26 (2010).
65. S. Spano, G. C. Cardarilli, L. di Nunzio, R. Fazzolari, D. Giardino, M. Matta, A. Nannarelli, M. Re, An efficient hardware implementation of reinforcement learning: The q-learning algorithm. *IEEE Access* **7**, 186340–186351 (2019).
66. Z. Wang, C. Li, W. Song, M. Rao, D. Belkin, Y. Li, P. Yan, H. Jiang, P. Lin, M. Hu, J. P. Strachan, N. Ge, M. Barnell, Q. Wu, A. G. Barto, Q. Qiu, R. S. Williams, Q. Xia, J. J. Yang, Reinforcement learning with analogue memristor arrays. *Nat. Electron.* **2**, 115–124 (2019).
67. Ł. Kuśmierz, T. Isomura, T. Toyoizumi, Learning with three factors: Modulating Hebbian plasticity with errors. *Curr. Opin. Neurobiol.* **46**, 170–177 (2017).
68. P. Mazzoni, R. A. Andersen, M. I. Jordan, A more biologically plausible learning rule for neural networks. *Proc. Natl. Acad. Sci. U.S.A.* **88**, 4433–4437 (1991).
69. R. Spanagel, F. Weiss, The dopamine hypothesis of reward: Past and current status. *Trends Neurosci.* **22**, 521–527 (1999).
70. L. Stein, J. Belluzzi, C. Wise, Benzodiazepines: Behavioral and neurochemical mechanisms. *Am. J. Psychiatry* **134**, 665–669 (1977).

Acknowledgments

Funding: This work was supported by Engineering and Physical Sciences Research Council (EPSRC) through Engineering Fellowship for Growth-neuPRINTSKIN (EP/R029644/1) and Hetero-print Programme Grant (EP/R03480X/1). **Author contributions:** F.L. and R.D. conceived the idea. F.L. and A.C. carried out the NW synthesis with the support from D.S. A.C. performed the NW contact printing. F.L. fabricated the devices both on rigid and flexible substrate. F.L. and S.D. performed the DC and pulse measurement of the devices. M.S.B. simulated and implemented the neuron circuit. F.L. and M.S.B. realized the tactile neural pathway with the help from S.D. M.C. realized the clock signal control of the system. R.C. carried out the robot control study and performed the neural network simulation. F.L. and R.D. wrote the paper. All authors provided comments and agreed with the final form of the manuscript. R.D. provided the overall supervision of the work. **Competing interests:** The authors declare that they have no competing interests. **Data and materials availability:** All data needed to evaluate the conclusions in the paper are present in the paper or the Supplementary Materials.

Submitted 1 August 2021
Accepted 5 May 2022
Published 1 June 2022
10.1126/scirobotics.abl7286

Science Robotics

Printed synaptic transistor–based electronic skin for robots to feel and learn

Fengyuan Liu, Sweety Deswal, Adamos Christou, Mahdieh Shojaei Baghini, Radu Chirila, Dhayalan Shakthivel, Moupali Chakraborty, and Ravinder Dahiya

Sci. Robot. **7** (67), eabl7286. DOI: 10.1126/scirobotics.abl7286

Science Robotics (ISSN 2470-9476) is published by the American Association for the Advancement of Science. 1200 New York Avenue NW, Washington, DC 20005. The title *Science Robotics* is a registered trademark of AAAS.